JOURNAL OF MATERIALS SCIENCE 37 (2002) 4165–4180

Numerical study of the time dependent behavior of GN-10 structural ceramics in bend creep test

J. L. DING
School of Mechanical and Materials Engineering, P. O. Box 642920, Washington State University, Pullman, WA 99164-2920, USA
E-mail: ding@mme.wsu.edu

Numerical simulation coupled with a realistic material model for high temperature structural ceramics is used to gain insight into the time dependent behavior of ceramics under bending. No simplifications used in conventional analysis methods are invoked, such as the assumption of steady-state creep and omission of elastic deformation etc. As yet, the formulation is shown to be sufficiently general to adopt arbitrary material models. The final formulation results in a set of first order coupled ordinary differential equations that can be solved with ease by well-established numerical techniques. Due to the time-dependent and inhomogeneous stress and strain distributions in the specimen, it is generally difficult to extract intrinsic material information associated with a particular stress state from the bend creep test. The validity of the material parameters obtained from bend creep tests depends on the validity of the assumptions that underlie the analysis. More *in situ* measurements to obtain information besides deflection, such as the location of the neutral axis etc., will be helpful for interpreting the bend test data. However, in this case, the major advantage of the bend test, namely, simplicity, is eradicated.

1. Introduction

Due to their many superior mechanical properties at high temperatures, e.g., high strength, low density, high oxidation resistance, and low coefficient of thermal expansion etc., silicon nitride (Si_3N_4), silicon carbide (SiC) ceramics and related composites have been the major candidates as high temperature structural materials. For high temperature applications, the time dependent deformation (creep) and fracture (creep fracture) are a major concern in design especially when stringent dimensional stability and design tolerance are required. The design database for creep and creep fracture must be derived based on intrinsic material behavior, which is determined directly by physical measurements but not indirectly by deduction based on theories. The case in point is the method of generating creep data by uniaxial testing versus that by 3-point or 4-point bend testing. Under uniaxial loading, a true uniform stress is induced in the test sample. Therefore the measured creep deformation represents the intrinsic material response to an unambiguously determined stress. On the other hand, the stress at any generic point in the bend specimen under a constant load varies with time, and can not be measured directly. Therefore the interpretation of the data has to rely on certain assumptions. However, because of the simplicity in specimen design, test setup, and low cost, bend test was used extensively in the past and has been continuously used to characterize the high temperature creep behavior of the structural ceramics. Some can be cited for the works by Chen and Chuang [1], Lin and Becher [2], Thayer and Yang [3], Salem and Choi [4], and Rendtel and Hübner [5] among others.

The typical assumptions underlying the analysis of the bend test data are that the creep behavior has reached steady state and follows power law model, e.g.,

$$\dot{\varepsilon}^c = A\sigma^n \tag{1}$$

where $\dot{\varepsilon}^c$ is the steady state creep rate, σ the stress, n (stress exponent) and A (pre-exponent constant) are the material constants. The objective of the bend test often emphasizes on the extraction of material constants in Equation 1. Since both tensile and compressive stresses are involved in a bend test, some further assumption on the symmetry between tension and compression creep also needs to be made. Assuming symmetrical behavior between tension and compression, i.e., A and n are the same for tension and compression, Hollenberg *et al.* [6], established a simple relation between the deflection of the specimen and the material constants A and n. This relation was used by Lin and Becher [2] to characterize the creep behavior of Alumina-SiC-whisker composites. To incorporate asymmetry in the analysis, Finnie [7] considered the case in which $A_t \neq A_c$, and $n_t = n_c = 1$ and obtained a closed form solution for the creep displacement in a bend test. His analysis was later extended by Talty and Dirks [8] for $n_t = n_c = N$ where N is an arbitrary number. The most general case, i.e., $A_t \neq A_c$, and $n_t \neq n_c$, was studied by Chuang [9]. For the symmetrical case, the neutral axis should stay the same as the central axis of the test beam. For the

asymmetrical case, the neutral axis is shifted to the compression side of the beam. However, because of the assumption of steady state, the position of the neutral axis and stress and strain fields are invariant with time [1, 9]. Other details of these analyses will be discussed later.

Some obvious issues associated with the various analysis methods mentioned above are: how valid the aforementioned assumptions are, how the determined material constants are affected by these assumptions, and how stress and strain evolve with time in the specimen during a bend test, etc. To try to experimentally resolve these issues will be very difficult if not impossible partially because of the very high temperatures involved in the bend creep test of structural ceramics. In this study, we try to use numerical simulations to address these issues. The objective is to gain a good insight into the time dependent behavior of ceramics under bending and shed light on the use of bend test to extract high temperature creep data for structural ceramics.

2. Deformation and life prediction model for GN-10 Si_3N_4 ceramic

2.1. Tension creep

Realistic numerical simulations require realistic material model. Nearly all the material models for high temperature structural ceramics are based on power-law creep as described by Equation 1. A more realistic deformation and life prediction model was developed by Ding *et al*. based on a systematic experimental investigation of the tensile creep and creep rupture of a grade of Si_3N_4, commercially designated as GN-10* [10]. The model was formulated using the state variable approach. Two internal state variables, namely a hardening variable (δ) and a damage variable (ω) were employed to characterize the current inelastic state of the material. The model consists of three equations, a flow rule, Equation 2 shown below, which describes the inelastic strain rate ($\dot{\varepsilon}^c$), a more generic term than "creep rate", as a function of the internal state variables, applied stress (σ), and temperature; and two evolution rules, Equations 3 and 4, for the two internal state variables. Specifically, the model is in the following form.

$$\dot{\varepsilon}^c = \frac{54^n \dot{\varepsilon}_0 \left(\frac{\sigma - \sigma_{\text{th}}}{54} - c\right)^n \mathrm{e}^{-\frac{Q_\varepsilon}{RT}}}{\delta} \tag{2}$$

$$\dot{\delta} = \frac{\dot{\delta}_0}{\delta^m} \mathrm{e}^{-\frac{Q_\delta}{RT}} \tag{3}$$

$$\dot{\omega} = \frac{\dot{\omega}_0 \left(\frac{\sigma}{54}\right)^\upsilon \mathrm{e}^{-\frac{Q_\omega}{RT}}}{\delta(1-\omega)} \tag{4}$$

where $\dot{\varepsilon}_0 = \mathrm{e}^{78.08}$ for $T \le 1200^\circ$C, $\mathrm{e}^{78.08}$ for $T > 1200^\circ$C; $\sigma_{\text{th}} = 1765.8 - 1.12T$ MPa for $T \le 1250^\circ$C, $516.9 - 0.3T$ MPa for $T > 1250^\circ$C; $\sigma_{\text{trans}} = 1848.3 - 1.12T$ MPa for $T \le 1250^\circ$C, $1108.1 - 0.634T$ MPa for $T > 1250^\circ$C; $c = 0, n = 1$ for $\sigma \le \sigma_{\text{trans}}$, $c = 1, n = 1.32$ for $\sigma > \sigma_{\text{trans}}$ and $T \le 1250^\circ$C, $c = 1$, $n = 1.7$ for $\sigma > \sigma_{\text{trans}}$ and $T > 1250^\circ$C; $Q_\varepsilon = 957.4$ kJ/mole for $T \le 1200^\circ$C , 270 kJ/mole for $T > 1200^\circ$C; $m = 1/3$; $\dot{\delta}_0 = \mathrm{e}^{93.5}$ for $T \le 1200^\circ$C , $\mathrm{e}^{-1.26}$ for $T > 1200^\circ$C; $Q_\delta = 1174$ kJ/mole for $T \le 1200^\circ$C, 13.26 kJ/mole for $T > 1200^\circ$C; $\dot{\omega}_0 = \mathrm{e}^{103.46}$, $\upsilon = 10.47$, and $Q_\omega =$ 149 kJ/mole; $\dot{\omega} = 0$ for $\sigma \le 0$. T is the absolute temperature in K, R is the gas constant, σ_{th} is the threshold stress below which creep is assumed to be negligible, and σ_{trans} is the transition stress from a linear to a nonlinear stress dependence of the inelastic strain rate. In terms of creep fracture, σ_{trans} is also the transition stress from the low-stress long-term creep to high-stress short-term creep.

Hardening of the material, which is characterized by δ, appears to be mainly due to a combination of the devitrification of the residual glass phase (GN-10 has a continuous glass film at the boundaries) as well as consequent phase transformations. The initial values for δ and ω are 1 and 0 respectively and both of them increase monotonically. The rupture is signified by $\omega = 1$ or $\dot{\omega} = \infty$. It should be noted that Equation 3 is coupled with Equations 2 and 4 respectively, but (2) and (4) are independent of each other. Therefore, what Equations 2 to 4 describe is essentially two independent processes, namely, creep deformation and fracture. Both processes can be impeded by the strengthening effect due to the hardening of the grain boundary phase. This fact can also be easily seen from the mathematical point of view as follows. Equation 2 can be integrated as:

$$\delta = \left[1 + (1+m)\dot{\delta}_0 \mathrm{e}^{-\frac{Q_\delta}{RT}}\right]^{\frac{1}{m+1}} \tag{5}$$

Substitution of Equation 5 into Equations 2 and 4 yields the following two independent equations for $\dot{\varepsilon}^c$ and $\dot{\omega}$ respectively.

$$\begin{aligned}\dot{\varepsilon}^c &= \frac{54^n \dot{\varepsilon}_0 \left(\frac{\sigma - \sigma_{\text{th}}}{54} - c\right)^n \mathrm{e}^{-Q_\varepsilon/RT}}{\left[1 + (1+m)\dot{\delta}_0 \mathrm{e}^{-Q_\delta/RT}\right]^{1/(m+1)}} \\ &= f(\sigma, T, t)\end{aligned} \tag{6}$$

$$\begin{aligned}\dot{\omega} &= \frac{\dot{\omega}_0 \left(\frac{\sigma}{54}\right)^\upsilon \mathrm{e}^{-\frac{Q_\omega}{RT}}}{\left[1 + (1+m)\dot{\delta}_0 \mathrm{e}^{-Q_\delta/RT}\right]^{1/(m+1)}(1-\omega)} \\ &= g(\sigma, T, t)\end{aligned} \tag{7}$$

Equations 6 and 7 also indicate that the model essentially follows the time-hardening rule. In addition to simplifying the model, decoupling of Equations 2 and 4, or equivalently, neglecting the possible interaction between damage and creep deformation, was based on the observation that at least for GN-10, fracture seems to be dominated by localized damage due to the growth of preexisting defects, rather than distributed damage caused by void nucleation, growth and coalescence even though the latter may operate concurrently. Other details of the model can be found in Ref. [10]. A comparison of the model and experimental data is shown in Fig. 1. In general, the creep data are

* GN-10 is a commercial grade of hot-isostatically-pressed Si_3N_4 ceramic containing small additions of Y_2O_3 and SrO as a densification aids, engineered by Garrett Ceramic Components Division of Allied-Signal Aerospace Company, Torrance, CA.

reproduced by the model reasonably well. The model was also demonstrated to give a reasonable description of the deformation and fracture behavior of GN-10 under constant strain-rate tensile loading [11]. The above scalar model can also be extended into a tensor form to incorporate the possible sensitivity of material behavior to pressure, dilatancy and compaction, asymmetry between tension and compression, and deformation induced hardening and softening [12].

In addition to the advanced model, the creep data shown in Fig. 1 were also analyzed using the traditional power law creep relation. To this end, the steady state creep rates need to be determined first. For a creep curve exhibiting three stages of creep, namely, primary, secondary, and tertiary creep, the steady state (secondary) creep rate can be determined unambiguously as the creep rate at the transition to tertiary creep. It is obvious that the steady state creep rate is also the minimum creep rate during the creep lifetime. However, the creep data shown in Fig. 1 shows neither tertiary creep nor appreciable steady state creep. Consequently, creep rates at rupture were used to characterize the power law relation. Including the temperature dependence, the relation was determined to be

$$\dot{\varepsilon}^c = e^{56}\sigma^{12.6}e^{-1645/RT} \tag{8}$$

The definitions and units of the symbols are the same as those used in Equations 2 to 4. In other words, the stress exponent is equal to 12.6. The number 1645 is in kJ/mole and usually termed as the activation energy [13].

2.2. Compression creep

To analyze bend specimen in creep, the creep behavior of the material in compression must be known. Fig. 2 shows sample of creep data of GN-10 Si_3N_4 tested at 1300°C in compression with a series of applied stresses beginning from −125 MPa [14], including a creep curve for a specimen tested in tension at 125 MPa (ruptured in 15.2 h) for comparison. The compressive stress was increased intermittently in steps of −25 MPa increment. The asymmetrical creep behavior in tension and compression is clearly discerned. The creep rate under a tensile stress of 125 MPa is significantly higher than that under the same stress in compression by about three orders of magnitude. Although tensile creep curves at

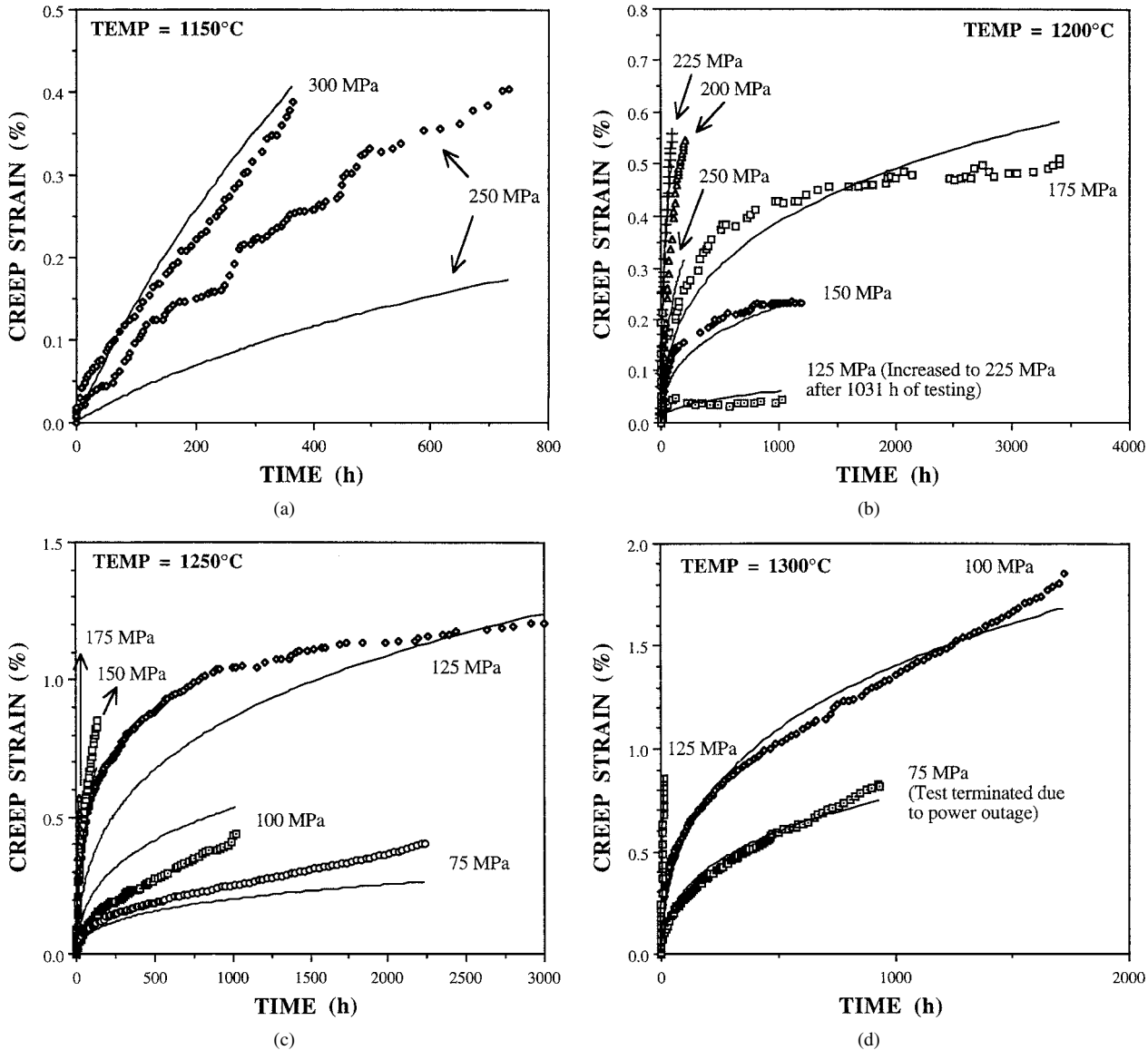

Figure 1 Creep data (symbols) and model predictions (solid lines) of GN-10 ceramic under uniaxial tensile loading: (a) 1150°C; (b) 1200°C; (c) 1250°C; (d) 1300°C.

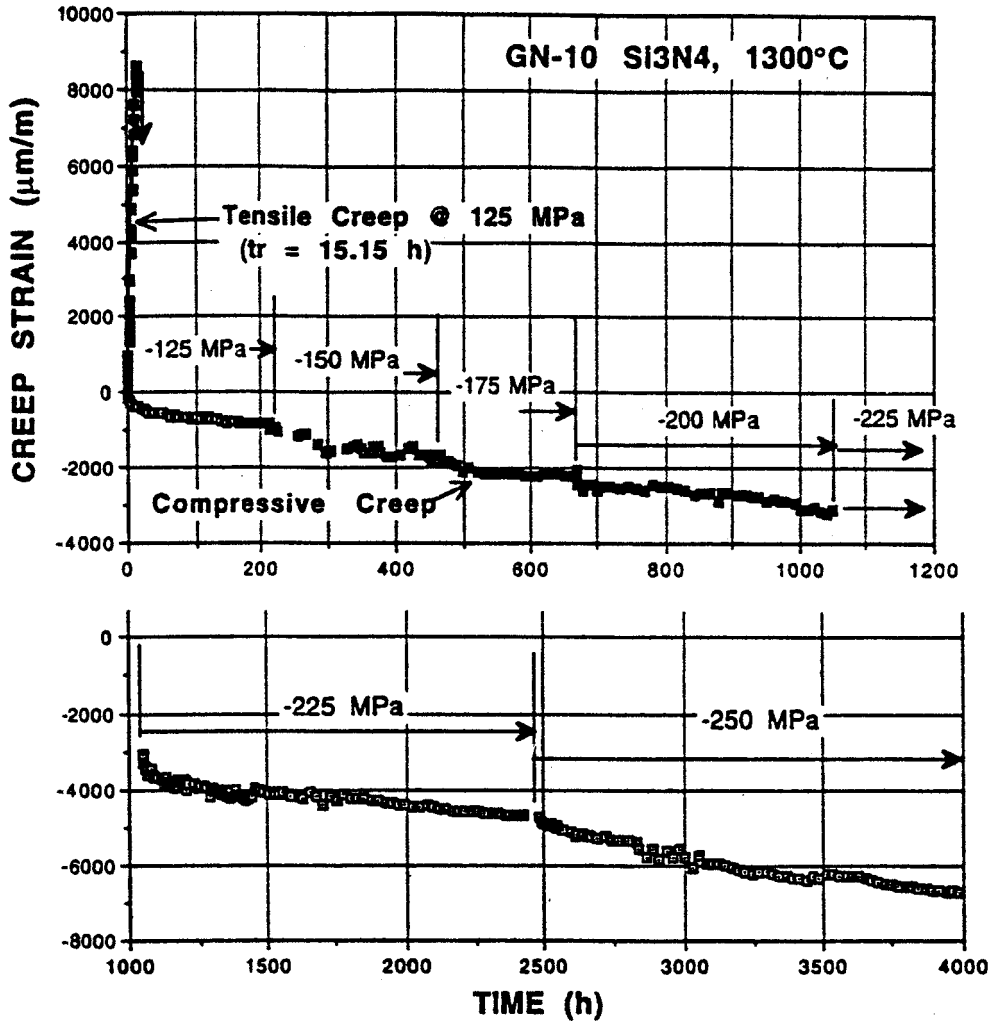

Figure 2 Creep curves of GN-10 Si_3N_4 tested in tension (ruptured in 15.2 h) and in compression at 1300°C. The compressive stress was increased intermittently in steps of −25 MPa from −125 MPa.

stresses above 125 MPa are not available for comparison, more severe contrast in creep behavior under tension and compression can be contemplated. Similar test was also performed on SN-88 Si_3N_4 by Yoon *et al.* [15].

As mentioned earlier, the scalar model described by Equations 2 to 4 can be extended into a tensor form to incorporate the asymmetry between tension and compression. However, characterization of a tensor model requires more sophisticated experimental data such as those on compression creep at various stress levels, creep under mixed loading, and deformation induced dilatancy etc. There are very few data available in this regard. Hence, in the following analysis, two extreme cases will be analyzed. One is that compression creep is assumed to be symmetrical with respect to tension creep. The other is to completely ignore the creep under compression. The real material behavior will be somewhere in between. However, for GN-10, the creep behavior is expected to be much closer to the latter as demonstrated in Fig. 2.

3. Formulation of the four point bending problem

A typical experimental setup for a four point bend test is shown in Fig. 3. The middle section between loading points B and C is subjected to constant bending moment. Therefore, the stress distribution on any plane normal to the beam axis is identical. The strain is calculated from the relative deflection at the middle of the span (U in Fig. 3) measured with respect to the line connecting the two loading points [2, 3]. A hypothetical specimen conforming to ASTM standard C1161, namely, $L = 40$ mm, 2 h (depth) = 3 mm is used in the following analyses. The length of the middle span (BC) is $L/2$. Since all the calculations are to be carried out in a "moment per unit thickness" basis, the thickness of the specimen is not involved in the analysis.

The total strain (ε^T) consists of inelastic or creep strain (ε^c) and elastic strain ($\varepsilon^e = \sigma/E$, where E is elastic modulus), i.e.,

$$\varepsilon^T = \varepsilon^e + \varepsilon^c = \sigma/E + \varepsilon^{\mathrm{c}} \tag{9}$$

Or in rate form,

$$\frac{\dot{\sigma}}{E} = \dot{\varepsilon}^T - \dot{\varepsilon}^c \tag{10}$$

Following the conventional assumption used in the simple beam theory, namely, plane sections remains plane during bending, ε^T is linearly distributed along the depth of the specimen as shown in Fig. 3, and can be written as

$$\varepsilon^T = \frac{z + c}{\rho} \tag{11}$$

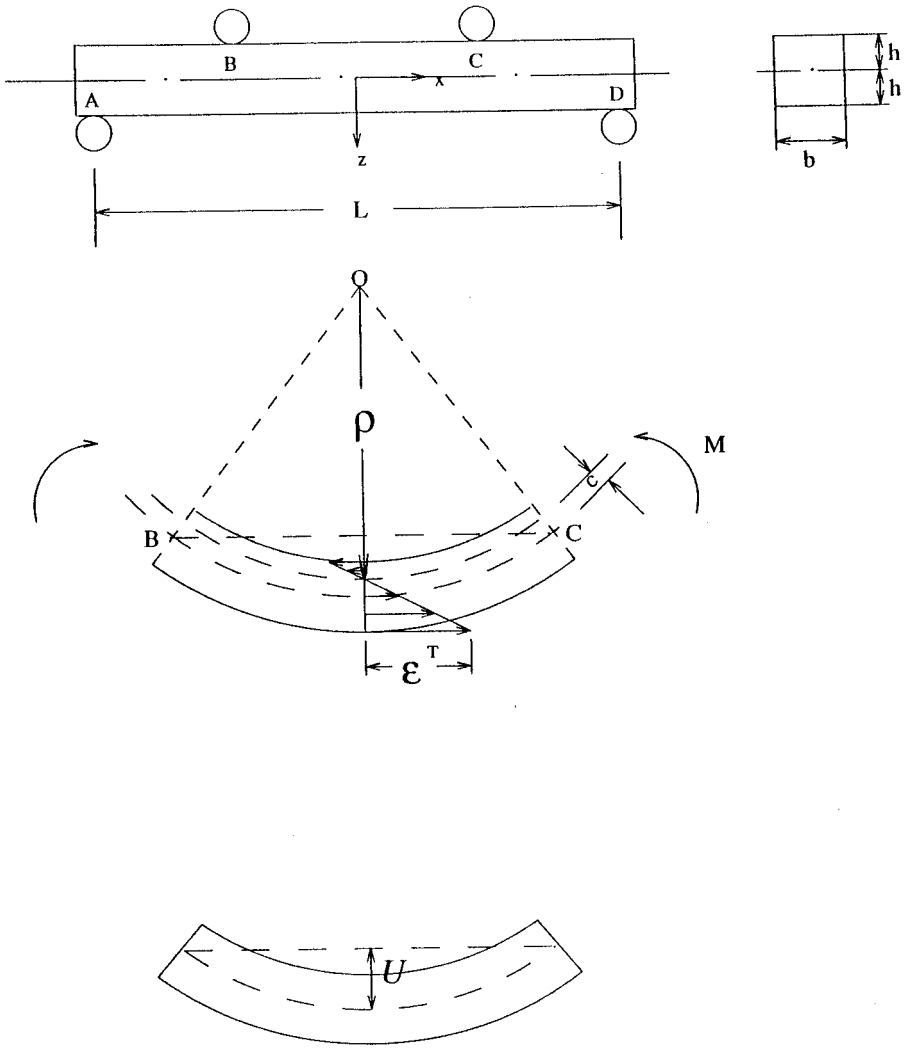

Figure 3 A schematic diagram of a typical four point bend test.

or

$$\dot{\varepsilon}^T = \frac{\dot{c}}{\rho} - \frac{(z+c)\dot{\rho}}{\rho^2} \tag{12}$$

where c is the distance between the central axis and the strain neutral axis along which the total strain is zero, z is the coordinate in the z direction with respect to a coordinate system whose origin is located at the center of the specimen (see Fig. 3), and ρ is the radius of curvature to the strain neutral axis. Substitution of Equation 12 into Equation 10 yields

$$\dot{\sigma} = E\left[\left(\frac{\dot{c}}{\rho} - \frac{(z+c)\dot{\rho}}{\rho^2}\right) - \dot{\varepsilon}^c\right] \tag{13}$$

The boundary conditions on either side B or side C are that the resultant force is equal to zero and the resultant moment is equal to the applied moment per unit thickness M, namely,

$$\int_{-h}^{h} \sigma \, \mathrm{d}z = 0, \quad \text{and} \quad \int_{-h}^{h} \sigma z \, \mathrm{d}z = M \tag{14}$$

In rate form, they can be written as

$$\frac{\mathrm{d}}{\mathrm{d}t}\int_{-h}^{h} \sigma \, \mathrm{d}z = \int_{-h}^{h} \dot{\sigma} \, \mathrm{d}z = 0, \quad \text{and} \quad \frac{\mathrm{d}}{\mathrm{d}t}\int_{-h}^{h} \sigma z \, \mathrm{d}z = \int_{-h}^{h} \dot{\sigma} z \, \mathrm{d}z = 0 \tag{15}$$

The time derivative in the second equation is equal to zero because M is a constant. Since z represents the coordinate of a material point with respect to the central axis, it does not change with time, i.e., $\dot{z} = 0$. The rate of neutral axis shift is given by $\dot{c}$. Substitution of Equation 13 into Equation 15 then leads to the following two equations,

$$\int_{-h}^{h}\left[\frac{\dot{c}}{\rho} - \frac{(z+c)\dot{\rho}}{\rho^2}\right]\mathrm{d}z = 2h\left[\left(\frac{\dot{c}}{\rho}\right) - \left(\frac{\dot{\rho}c}{\rho^2}\right)\right] = \int_{-h}^{h} \dot{\varepsilon}^c \, \mathrm{d}z = \int_{-h}^{h} f(\sigma, T, t; z) \, \mathrm{d}z = A \tag{16}$$

and

$$\int_{-h}^{h}\left[\frac{\dot{c}}{\rho} - \frac{(z+c)\dot{\rho}}{\rho^2}\right]z \, \mathrm{d}z = -\frac{2h^3}{3}\left(\frac{\dot{\rho}}{\rho^2}\right) = \int_{-h}^{h} \dot{\varepsilon}^c z \, \mathrm{d}z = \int_{-h}^{h} f(\sigma, T, t; z) z \, \mathrm{d}z = B \tag{17}$$

respectively. The parameter z is included in the function f to indicate the inhomogeneous stress distribution and the corresponding creep rate across the depth of the specimen. From the above two equations, $\dot{\rho}$ and $\dot{c}$ can be solved as

$$\dot{\rho} = -\frac{3}{2h^3}\rho^2 B \tag{18}$$

$$\dot{c} = \rho\left[\frac{A}{2h} - \frac{3}{2h^3}Bc\right] \tag{19}$$

Equations 13 and 7 can also be rewritten as

$$\dot{\sigma} = E\left[\left(\frac{A}{2h} - \frac{3}{2h^3}Bc + \frac{3(z+c)}{2h^3}B\right) - f(\sigma, T, t; z)\right] \tag{20}$$

$$\dot{\omega} = g(\sigma, T, t; z) \tag{21}$$

In the following analysis, σ and ω are evaluated at 21 equally spaced (0.15 mm apart) points across the depth. Therefore, Equations 18 to 21 constitute a set of 44 coupled first order ordinary differential equations for the evolution of ρ, c, σ and ω. The numerical scheme for solving these type of equations has been well established. To complete the formulation, the initial conditions have to be specified. They are zero for c and ω. The initial conditions for σ and ρ are the initial elastic stress distribution, namely, $\sigma = (Mz)/I$, where I is the moment of inertia, and $\rho_0 = EI/M$ respectively. Based on the specimen geometry shown in Fig. 3, the relation between the moment per unit thickness, M in Newtons, and the initial elastic stress along outside fiber, σ_0 in MPa, is $M = 1.5\ \sigma_0$. The center deflection relative to the two loading points B and C, i.e., U in Fig. 3, can be found from the deflection-curvature relation for a simple beam undergoing small deflection, namely,

$$\frac{\mathrm{d}^2 z}{\mathrm{d}^2 x} = \frac{1}{\rho + c} \tag{22}$$

"Small deflection" is a very legitimate assumption for bending of brittle materials. Equation 22 can be integrated to obtain

$$U = \frac{L^2}{32(\rho + c)} \tag{23}$$

and

$$\frac{\mathrm{d}U}{\mathrm{d}t} = -\frac{L^2}{32}\left[\frac{\dot{\rho} + \dot{c}}{(\rho + c)^2}\right] \tag{24}$$

The above deflection formulae were for the central axis of the specimen.

Since the above formulation does not invoke any simplified assumptions, its solution should represent a reasonably realistic simulation of the bend test. With the inclusion of the damage variable (ω), the rupture time can also be estimated. Furthermore, the formulation is not limited to any specific material model. Different deformation and damage models only affect the forms of functions f and g defined in Equations 6 and 7.

The correlation between the above general formulation and other analysis methods mentioned in the Introduction is discussed in the following.

3.1. Hollenberg *et al.*'s analysis [6]

The assumption of symmetry in tensile and compressive creep mandates that the neutral axis remains in coincidence with the central axis of the specimen or $c = 0$. The existence of steady state creep further asserts that the stress distribution remains unchanged with time; therefore, the elastic strain rate must be zero. With the aid of the power law equation, Equation 12 reduces to

$$\dot{\varepsilon}^T = \dot{\varepsilon}^c = -\frac{\dot{\rho} z}{\rho^2} = A\sigma^n \tag{25}$$

where $\dot{\rho} < 0$. In the region where $z > 0$, $\dot{\varepsilon}^c > 0$ and $\sigma > 0$; and where $z < 0$, $\dot{\varepsilon}^c < 0$ and $\sigma < 0$. For either case, σ can be written as

$$|\sigma| = \left(-\frac{\dot{\rho}}{A\rho^2}\right)^{1/n} |z|^{1/n} \tag{26}$$

The first equation of Equation 14 is automatically satisfied. The second one leads to

$$\left(-\frac{\dot{\rho}}{A\rho^2}\right)^{1/n}\left(\frac{2n}{2n+1}\right)h^{2+\frac{1}{n}} = M \tag{27}$$

With the aid of Equation 24 and $c = \dot{c} = 0$, Equation 27 can be written in the following logarithmic form as

$$\log\left(\frac{\mathrm{d}U}{\mathrm{d}t}\right) + \log\left[\frac{32}{AL^2}\left(\frac{2n}{2n+1}\right)^n h^{2n+1}\right] = n\log M \tag{28}$$

On the log-log plot of $\mathrm{d}U/\mathrm{d}t$ versus M, the values of n is determined from the slope of Equation 28 and A from the intercept. Equations 27 and 28 indicate that when M remains constant with respect to time, the rate change of the curvature and U are also constant, and the constant stress distribution is thereby implied by Equation 28.

3.2. Chuang's analysis [1, 9]

Chuang *et al*. assumed that $c \neq 0$, but $\mathrm{d}c/\mathrm{d}t = 0$. Therefore, Equation 12 becomes

$$\dot{\varepsilon}^c = -\frac{\dot{\rho}(z + c)}{\rho^2} \tag{29}$$

Furthermore, tensile creep and compressive creep are assumed to follow different power law relations, i.e.,

$$\dot{\varepsilon}^c = A_t\sigma^{n_t} \tag{30}$$

for tension, and

$$\dot{\varepsilon}^c = -A_c|\sigma|^{n_c} \tag{31}$$

for compression. In the region where $z > -c$, $\dot{\varepsilon}^c > 0$, and

$$\sigma = \left[-\frac{\dot{\rho}(z+c)}{A_t \rho^2} \right]^{1/n_t} \tag{32}$$

and in the region where $z < -c$, $\dot{\varepsilon}^c < 0$, and

$$\sigma = -\left[\frac{\dot{\rho}(z+c)}{A_c \rho^2} \right]^{1/n_c}. \tag{33}$$

Substitution of Equations 32 and 33 into Equation 14 then leads to the following two equations:

$$-\left[-\frac{\dot{\rho}}{\rho^2 A_c} \right]^{\frac{1}{n_c}} \int_{-h}^{-c} [-(z+c)]^{1/n_c} \, dz + \left[-\frac{\dot{\rho}}{\rho^2 A_t} \right]^{\frac{1}{n_t}} \int_{-c}^{h} [(z+c)]^{1/n_t} \, dz = 0 \tag{34}$$

$$-\left[-\frac{\dot{\rho}}{\rho^2 A_c} \right]^{\frac{1}{n_c}} \int_{-h}^{-c} [-(z+c)]^{1/n_c} z \, dz + \left[-\frac{\dot{\rho}}{\rho^2 A_t} \right]^{\frac{1}{n_t}} \int_{-c}^{h} [(z+c)]^{1/n_t} z \, dz = M \tag{35}$$

where

$$\int_{-h}^{-c} [-(z+c)]^{1/n_c} \, dz = \frac{n_c}{n_c+1} (h-c)^{\frac{n_c+1}{n_c}}$$

$$\int_{-c}^{h} [(z+c)]^{1/n_t} \, dz = \frac{n_t}{n_t+1} (h+c)^{\frac{n_t+1}{n_t}}$$

$$\int_{-h}^{-c} [-(z+c)]^{1/n_c} z \, dz = -\frac{n_c}{2n_c+1} (h-c)^{\frac{2n_c+1}{n_c}} - \frac{cn_c}{n_c+1} (h-c)^{\frac{n_c+1}{n_c}}$$

and

$$\int_{-c}^{h} [(z+c)]^{1/n_t} z \, dz = -\frac{n_t}{2n_t+1} (h+c)^{\frac{2n_t+1}{n_t}} - \frac{cn_t}{n_t+1} (h+c)^{\frac{n_t+1}{n_t}}$$

Since all the four integrals are independent of time, $\dot{\rho}/\rho^2$ and stress distribution are also independent of time.

Equations 34 and 35 involve six unknowns, namely, $\dot{\rho}/\rho^2$, c, A_t, A_c, n_t and n_c. To apply these equations to determine the creep parameters, two approaches were proposed [1]. The first approach employed direct numerical fitting of $\dot{\rho}/\rho^2$, which can be determined by the measured load point displacement rate, by Equations 34 and 35. This process is an iterative and tedious process. The second approach was to measure c using two columns of fiducial marks indented on the side of the specimen. With c and $\dot{\rho}/\rho$ measured, Equations 34 and 35 only involve four unknowns. Since one experiment generates one unique set of Equations 34 and 35 after c and $\dot{\rho}/\rho$ are replaced by the measured values, two experiments will provide four equations for four unknowns. However, these four equations can still not be solved analytically unless some further assumption and simplification are made [1, 16].

4. Simulated material behavior under four point bending

To understand the behavior of structural ceramics under bending and address the issues mentioned in the Introduction section, we first carry out a detailed analysis for the hypothetical beam subjected to four-point bending at 1300°C. The bending is assumed to induce elastic stresses of ±125 MPa at the outer chords before creep commences. Results are presented in physical quantities instead of normalized ones as used by Chuang [1, 9], Finnie [7] and others. Making use of the parametric values given in earlier sections, Equations 6 and 7 can be written respectively as

$$\dot{\varepsilon}^c = \frac{\alpha}{(1+0.137t)^{0.75}} \tag{36}$$

and

$$\dot{\omega} = -\frac{1.13 \times 10^{-23} \sigma^{10.47}}{(1+0.137t)^{0.75}(1-\omega)} \tag{37}$$

respectively, where $\alpha = 3.585 \times 10^{-6}(\sigma - 99)^{1.7}$ for $\sigma > 110.8$ MPa; $3.585(\sigma - 45)$ for $45 \le \sigma \le 110.8$ MPa; and 0 for $\sigma \le 45$ MPa. To investigate the effects of material model on the simulated test results, power law creep model, namely, Equation 8, was also studied. Hereafter, the model represented by Equations 2 to 4 or 6 and 7 will be referred as the advanced model. For each model, two cases, namely symmetrical and asymmetrical, were considered. For the asymmetrical case, $\dot{\varepsilon}^c = 0$ whenever $\sigma \le 0$; and for the symmetrical case, compressive creep and tensile creep are of the same magnitude but opposite signs. As mentioned earlier, these two cases represent two extremes. The actual response will be somewhere in between depending on the amount of compression creep. Since GN-10 appears to creep very little under compression, the results from the simulation based on asymmetrical, advanced model is expected to be close to reality.

The relative deflection, U, for the inner span is simulated based on four different combinations of the material models. Results are shown in Fig. 4. Case (a) is predicted based on symmetric power-law creep in tension/compression, case (b) asymmetric power-law creep, case (c) symmetric creep governed by the advance model, and case (d) asymmetric creep governed by the advanced model. Stress and damage profiles at various times are predicted based on the above four conditions and compiled in Figs 5 and 6 respectively. In cases (a) and (c), the neutral axis stays coincident with the central axis of the specimen, i.e., $c = 0$, as shown in Fig. 5a and c. In cases (b) and (d), the redistribution of the internal stresses (Fig. 5b and d) and consequential shifting of the neutral axis (shown in Fig. 7) are prompted by rapid relaxation of the high initial tensile stresses occurring in the outer chord region in compliance to the premise that planes normal to the central axis must remain plane during bending. The two c-curves shown in Fig. 7 are characteristically similar,

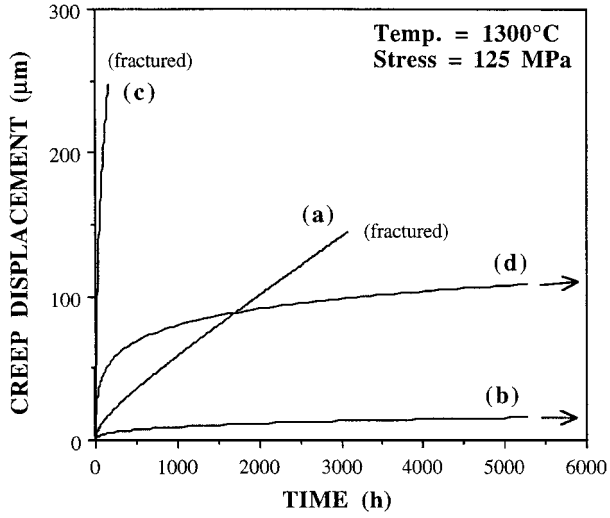

Figure 4 Simulated creep displacement for a four point bend specimen subjected to an initial elastic stress of 125 MPa and 1300°C: (a) symmetrical power law creep (b) asymmetrical power law creep (c) symmetrical creep governed by advanced model (d) asymmetrical creep governed by advanced model.

but differ in magnitude because the creep rate at any given stress governed by Equation 8 is always lower than that by Equation 36 at the same stress level during primary creep period, which is absent in the power-law model.

The rate of stress redistribution also has strong effects on the rupture life of the test specimen. According to Equation 4, only tensile stress will induce damage. Therefore, the faster the tensile stress is relaxed, the less damage the material incurs. This can be seen from the damage distribution curves shown in Fig. 6 for cases (b) and (d). Although the specimen for case (b) suffers more damage than that for case (d), both specimens survive even after about 10 years (87,840 h) according to the simulation. For cases (a) and (c), because of the symmetrical compressive creep, the tensile stress relaxation is much slower than cases (b) or (d). Consequently, the creep rupture lives are much shorter, 172 h and 3084 h for (a) and (c) respectively.

As mentioned earlier, one underlying assumption adopted in the currently existing analyses for bend creep

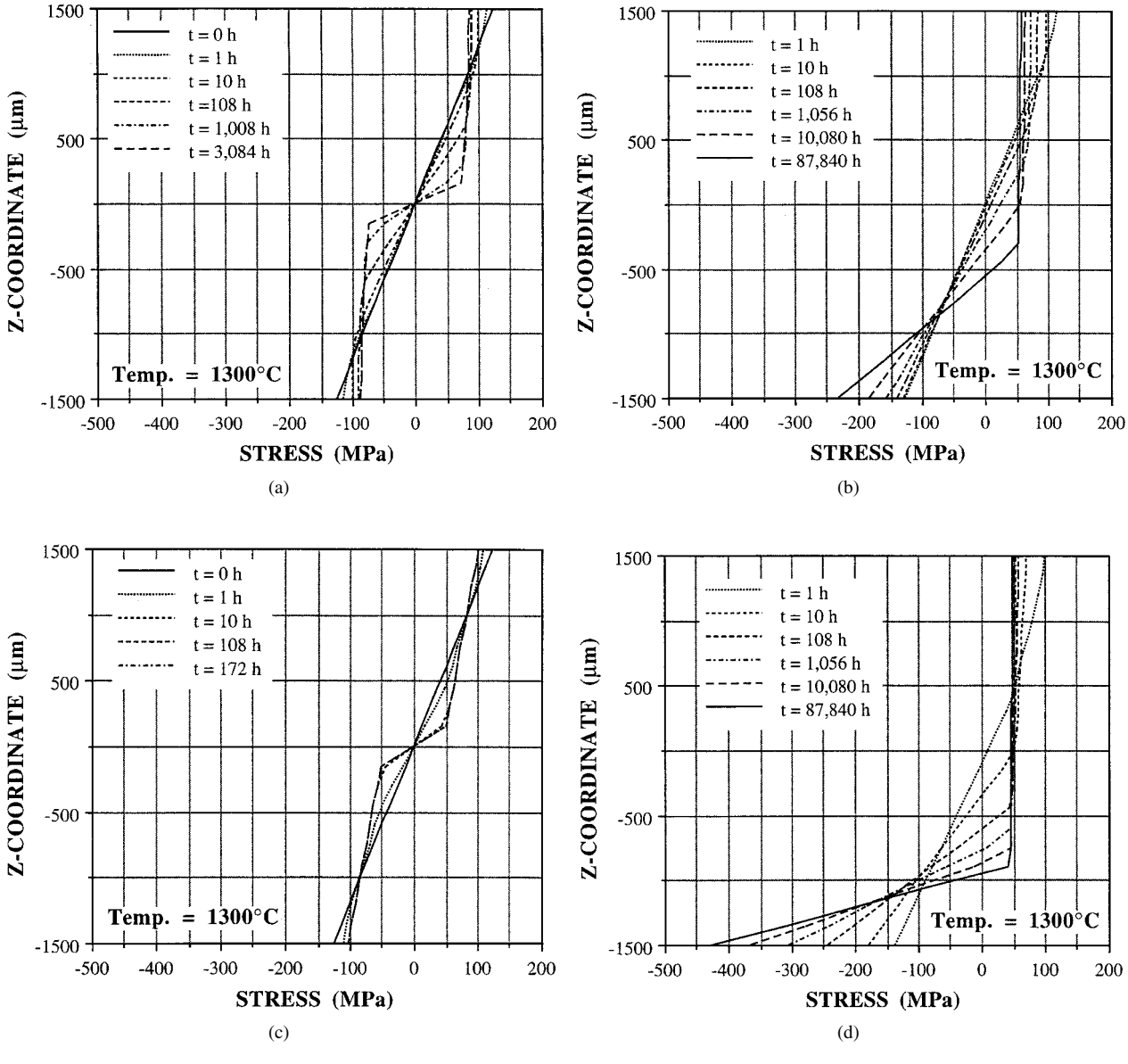

Figure 5 The stress distribution as a function of time for a four point bend specimen subjected to an initial elastic stress of 125 MPa and 1300°C: (a) symmetrical power law creep (b) asymmetrical power law creep (c) symmetrical creep governed by advanced model (d) asymmetrical creep governed by advanced model.

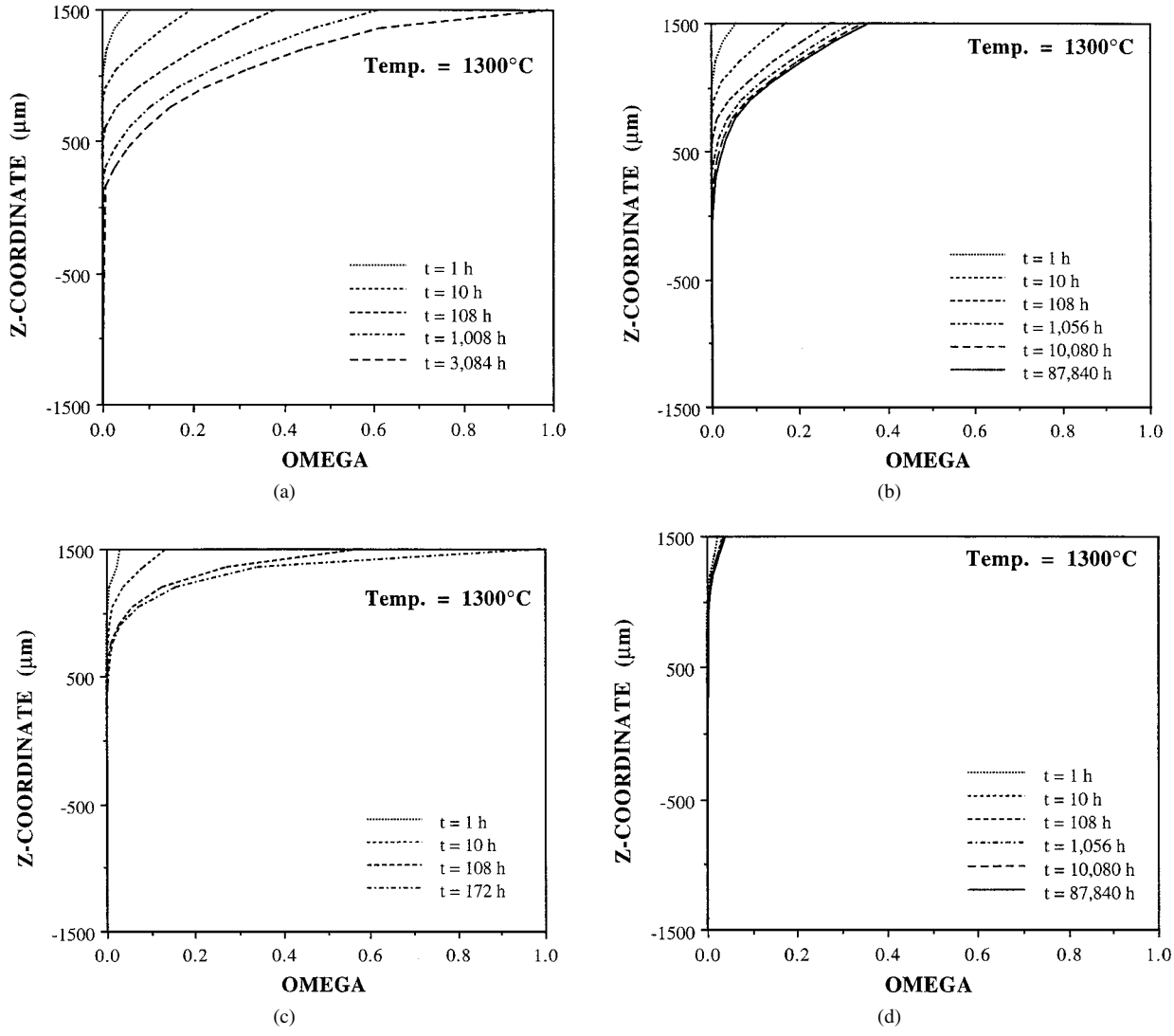

Figure 6 The distribution of ω (omega) as a function of time for a four point bend specimen subjected to an initial elastic stress of 125 MPa and 1300°C (a) symmetrical power law creep (b) asymmetrical power law creep (c) symmetrical creep governed by advanced model (d) asymmetrical creep governed by advanced model.

test is the existence of a steady state at which the stress distribution is invariant with time. Based on the current simulation, such state may be possible if the material itself does have a steady state and creep is symmetrical, i.e., case (a). The existence of steady state for this case is evidenced by the linear relationship between creep displacement and time, i.e., constant rate, as shown in Fig. 4. The attainment of steady state requires both the material behavior and stress distribution be steady. Thus, in a strict sense, the steady state does not exist in other cases. In order to satisfy the requirement that planes remains plane, whenever there is creep in the tension side, the compression side has to deform proportionally. For the asymmetrical cases, since there is little creep under compression, the only way to deform the specimen in the compression side is by the elastic deformation introduced by the increase of the compressive stresses. Consequently, the stress distribution has to keep changing, i.e., unsteady. This can be roughly seen from Fig. 7 which shows that the neutral axis is continuously shifting even after 10 years (87,840 h). For case (c), creep is symmetrical. However, because the creep model does not prescribe steady state creep behavior, the steady state can not be reached from the theoretical point of view. Despite of the lack of mathematical steady state, curves (b), (c), and (d) do show some apparent steady state because the transition rate at the later stage of the simulation is very small. Experimentally,

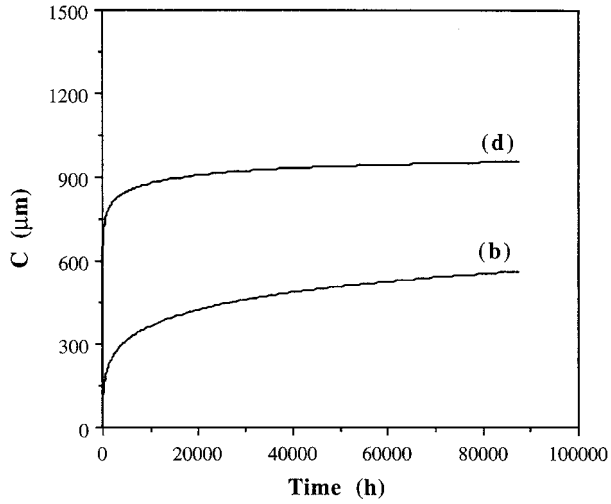

Figure 7 Shift of the neutral axis as a function of time for cases (b) and (d). See the captions of Figs 4 to 6. Notice that for the symmetrical cases (a) and (c), the neutral axis remains to be the same as the central axis of the specimen, i.e., $c = 0$.

the limitation on the resolution of instruments may also result in an apparent steady state. More discussion on steady state creep will be given in the next section.

It should also be noted that Equation 9, does not mandate that σ must be zero when ε^T is zero. In other words, the strain neutral axis may not coincide with the stress neutral axis in general. However, if the material does not creep or creeps very little under compression as assumed in cases (b) and (d), then these two axes should coincide because $\varepsilon^T = \varepsilon^e$ in the compression side. The deviation of the strain neutral axis from stress neutral axis from stress neutral axis was also noted and discussed in [17].

5. Estimation of creep exponents from simulated results

As mentioned earlier, extraction of stress exponent, n, and activation energy, Q, is usually the main purpose of the bend creep test. The known inputs for these tests are typically the applied bending moment and measured beam deflection. Little is known on the internal stress and strain distribution in the specimen. In this section, we will first use numerical simulation to generate a set of creep displacement curves for the aforementioned hypothetical specimen under various stresses and temperatures. We then use these simulated creep curves as the input to extract n and Q. Unlike physical bending experiments, we have complete knowledge about the input including the stress and strain evolution in the specimen for these virtual experiments. Thus, it's possible to gain good insight into the correlation between the outputs, e.g., n and Q, and the inputs using the knowledge developed in previous sections. This objective can be achieved without the necessity of using complicated analysis such as that proposed in [1, 16]. In fact, a simpler analysis will be easier to reveal the correlation between the input and output. In this regard, Hollenberg's approach for extracting n and Q is used in this study.

To estimate the stress exponent, a family of creep curves under various initial elastic stress distributions are needed. Shown in Fig. 8a are simulated creep curves at 1300°C calculated based on the advanced model with the asymmetrical creep behavior illustrated in case (d) study. The long-term creep curves with initial stresses below 175 MPa are plotted in Fig. 8a, showing no rupture occurring within 87,840 h. The short-term creep data up to 312 hours are shown in Fig. 8b. The rupture lives at 200 MPa and 225 MPa were calculated to be 6.09 h (shown in Fig. 8b) and 0.02 h respectively. The latter suggests that the flexural rupture strength at 1300°C would be slightly above 225 MPa. This value is comparable to the uniaxial fast fracture strength (199 MPa) estimated from the advanced model and experimental values (256 and 270 MPa) obtained from uniaxial tensile tests with a loading rate of 7.5 MPa/m [11]. The stress profiles under the six initial stresses and their subsequent redistribution at a few selected times are depicted in Fig. 9. Interestingly, the redistribution tends to flatten the tensile stress profiles into a trapezoidal profile with a height of about 45 MPa, which by no coincidence is the threshold stress at 1300°C. No

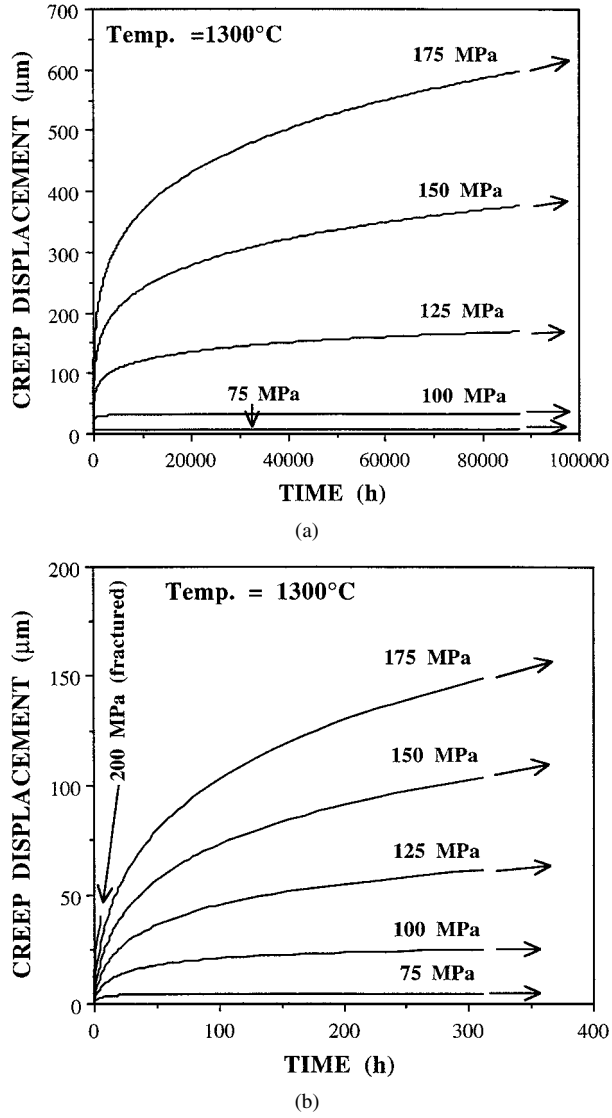

Figure 8 The simulated creep curves at 1300°C based on the advanced model and asymmetrical creep: (a) the creep data simulated up to 87,840 h; (b) the early stage of the simulated creep data (up to 312 hours).

creep occurs at or below the stress according to Equation 36. Failure to ease the high tensile stress in the 200 MPa test leads to the short rupture life. The shifting of the stress neutral axis and the resulting increase in the compressive stress are dramatic with increase of applied bending moment, as shown in Fig. 9g. The above analyses illustrate that bending creep curves that describe the change of relative deflection U with time can not be easily converted in the form of uniaxial creep curves because of stress relaxation and shifting of the stress and strain neutral axes. The situation is further complicated by the lack of true steady-state creep as discussed in three case studies (b) to (d), except in case (a).

In what follows, an attempt will be made to examine if any commonality or commutative relationship exists between the stress exponent determined from bend creep curves and that from uniaxial creep curves. To do so, the steady state creep rates need to be determined as function of stress and temperature. As mentioned earlier, the steady state creep rate is not well defined for a creep curve which shows neither tertiary creep nor appreciable steady state creep. Hence creep rate at rupture, or at the end of the creep curve, was used to characterize power law creep relation in [13].

Typically, 4-point bend tests are short, often failed in 100 h or less [2–5] or being discontinued after completing several hundreds hours of testing because the deflection creep curves often hint some appearance of linear behavior due to the limitation of the sensitivity of the deflection measurement equipment. LVDT (linear variable differential transformer) that is often used to measure the deflection has a typical resolution of ± 2 μm [1]. To examine the possible effect of creep duration on the values of n and Q, two sets of creep rates were determined based on the short-term (<312 h) and long-term (<87,400 h) creep curves shown in Fig. 8a and b, respectively. In Fig. 8a, apparent linear behavior is discernible in creep curves beyond about 200 h. However, these creep curves remain quite transient in a smaller time scale as shown in Fig. 8b. Both the short and long-term creep rates are plotted in Fig. 10. The data do not all fall on straight lines. Nevertheless, a linear relationship is usually established from experimental bend data that often poise the characteristic features similar to the filled data. Experimentally, the unfilled data points located in the lower left corner of Fig. 10 may be not obtainable due to uncertainty and limitations in deflection measurement instrument. A creep rate of 10^{-5} μm/h produces a deflection about 1 μm in 10 years, well within the resolution of the LVDT. The unfilled square data point at the upper right corner of Fig. 10 represents stress-rupture which is categorically different from creep rupture being consider here. The creep exponents, n, are estimated to be 4.7 and 5.2 based on the short-term and long-term filled data, respectively.

Despite that the creep rates determined from the short-term creep curves differ substantially from those of the long-term creep curves by two orders of magnitude as indicated in Fig. 10, the two n values show a remarkable agreement. The reason for this agreement can be understood more easily if the three creep curves simulated for 125, 150, and 175 MPa loading (the filled data in Fig. 10) are replotted in a log-log scale as shown in Fig. 11. As a first approximation, the curves beyond 100 h can be approximated with three parallel lines with a slope less than 1. These observations signify two things. Firstly, it implies that the displacement versus time data beyond 100 h can be described by $U = m_t k$,where k is a constant. Because all the three

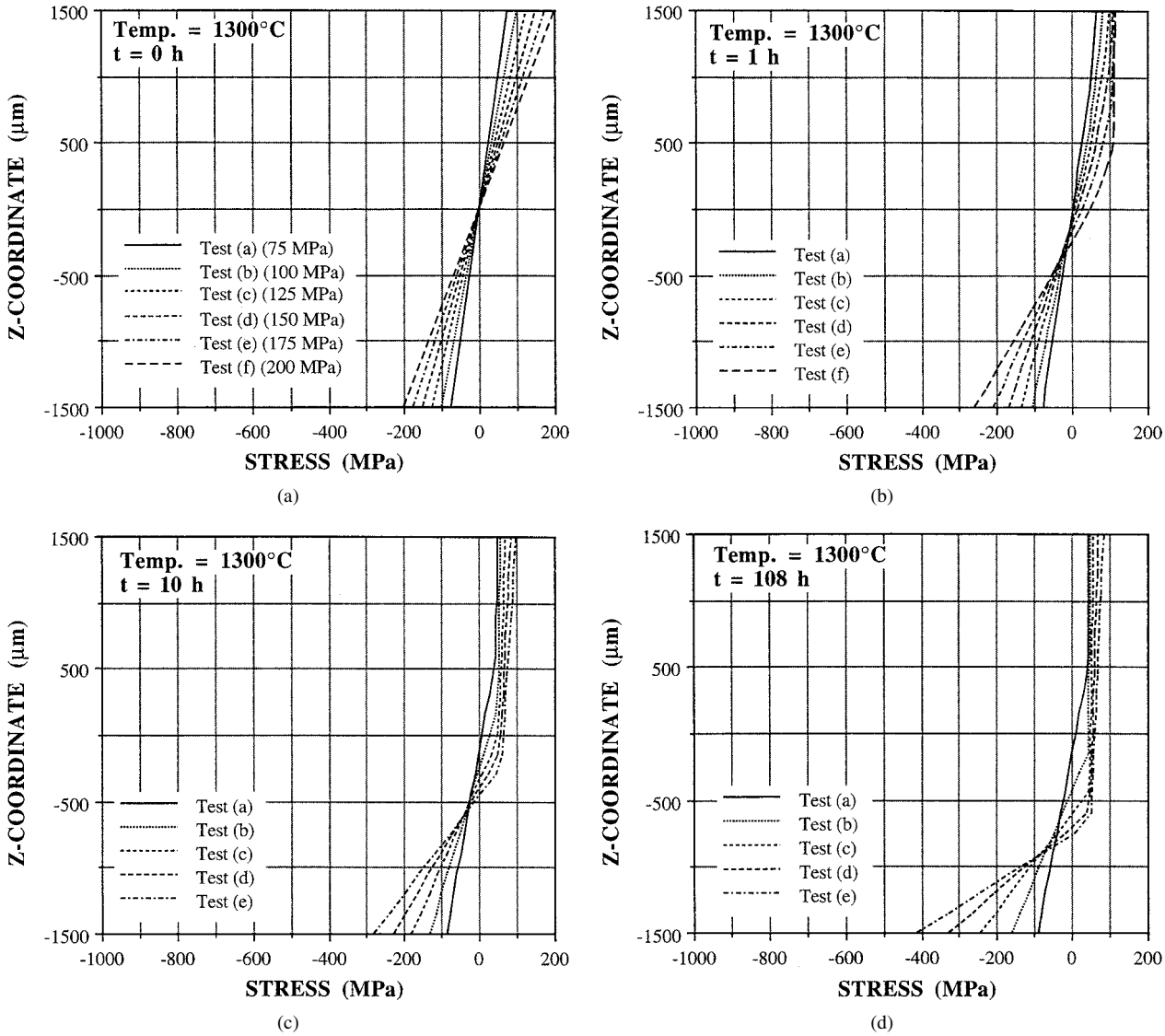

Figure 9 Stress redistribution during a four point bend test at 1300°C for various initial elastic stress distributions: (a) 0 h; (b) 1 h; (c) 10 h; (d) 108 h; (e) 1,056 h; (f) 10,080 h; (g) 87,840 h. (*Continued.*)

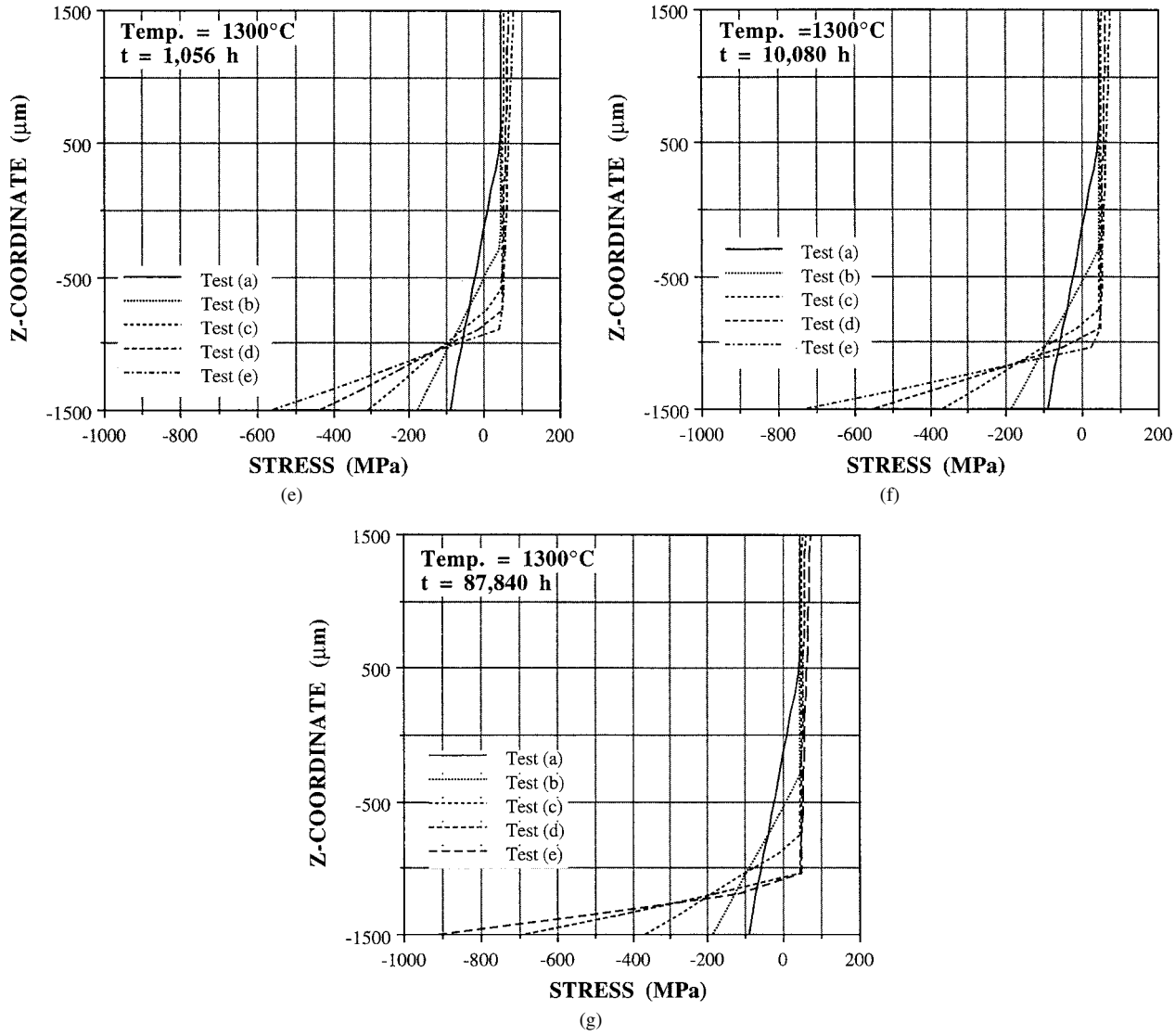

Figure 9 (*Continued*).

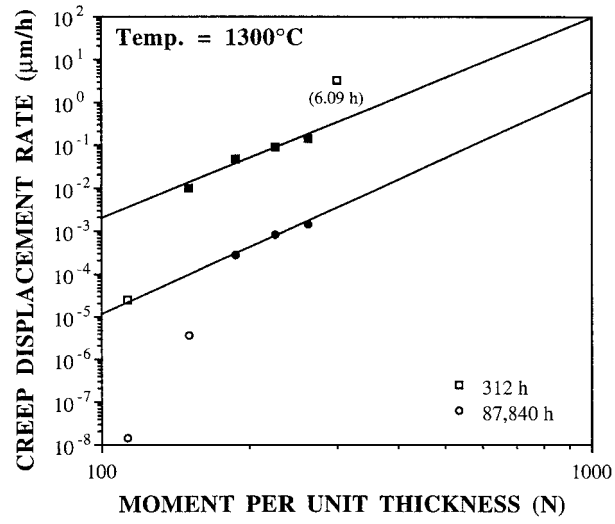

Figure 10 Simulated creep displacement rates, based on the advanced model combined with asymmetrical creep, as a function of the applied moment at 312 h and 87,840 h respectively. The slopes, i.e., the creep exponent for Equation 28, based on the filled data were estimated to be 4.7 and 5.2 for 312 h and 87,840 h respectively.

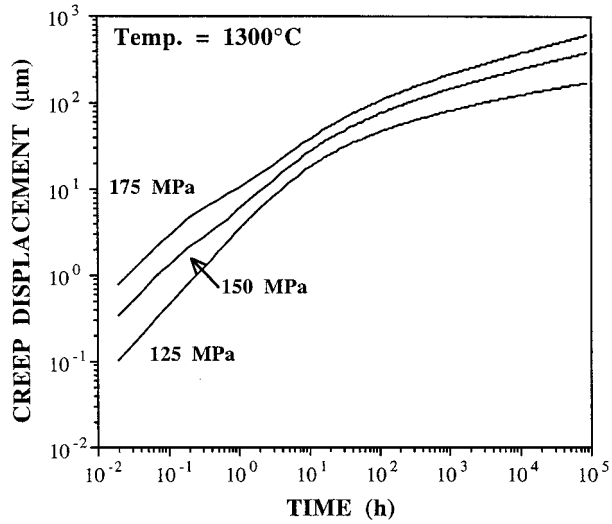

Figure 11 Simulated creep displacement based on the advanced model combined with asymmetrical creep as a function of time in a log-log scale. See Fig. 8a.

lines are parallel to each other, the ratio of any two displacement rates at any given time must be independent of time. Secondly, good fit of the displacement data by a power function of time with an exponent other than unity indicates the absence of steady state creep. From the physical point of view, the insensitivity of n to time may indicate that the creep characteristics at 312 hour and 87840 hour are similar. This may be reasonable because bend specimen with strong compression creep

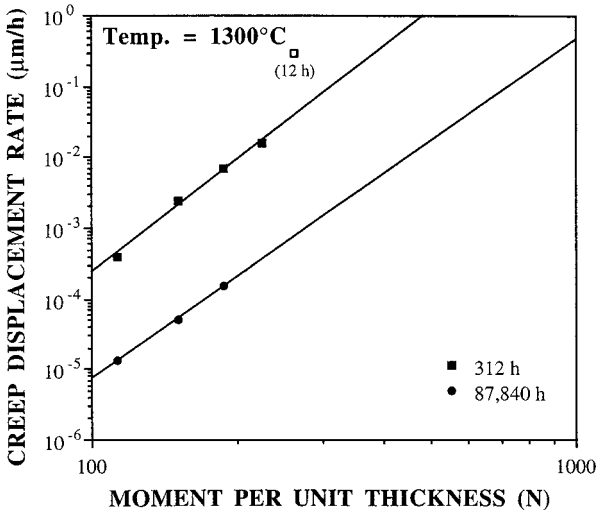

Figure 12 Simulated creep displacement rates, based on the power law creep model combined with asymmetrical creep, as a function of the applied moment at 312 h and 87,840 h respectively. The slopes, i.e., the creep exponent for Equation 28, based on the filled data were estimated to be 5.3 and 4.8 for 312 h and 87,840 h respectively.

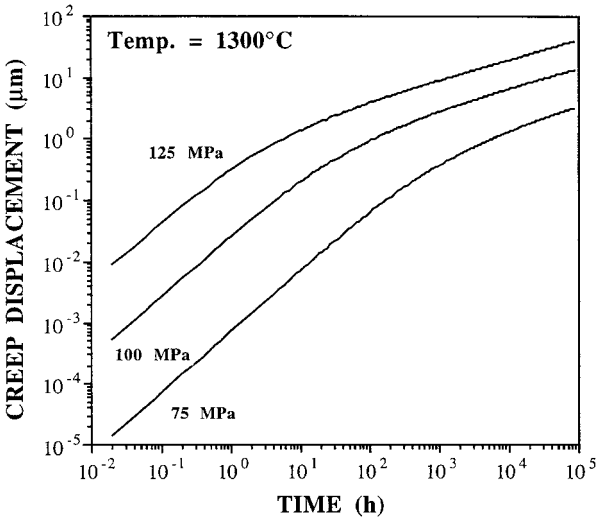

Figure 13 Simulated creep displacement based on the power law creep model combined with asymmetrical creep as a function of time in a log-log scale.

resistance does not creep much after a few hundred hours.

The creep displacement rates corresponding to the filled data shown in Fig. 10 are also simulated for the case (b) condition and plotted in Fig. 12 using the same legend. Again, two values of creep exponent n are estimated to be 5.3 and 4.8 for short- and long-term creep curves, respectively. These values agree well not only mutually but to those estimated in case (d) condition. The displacement rates for the three filled circular symbols shown in Fig. 12 versus time are plotted in log-log diagram shown in Fig. 13. The creep curves beyond 100 h can again be approximated with three parallel lines having a common slope of 0.34 to 0.39. The similarity between case (d) and (b) is likely to be also due to the strong compression creep resistance mentioned earlier.

To examine the effects of temperature dependence, creep curves at three temperatures of 1150, 1200, and 1250°C are simulated and shown in Fig. 14, using case

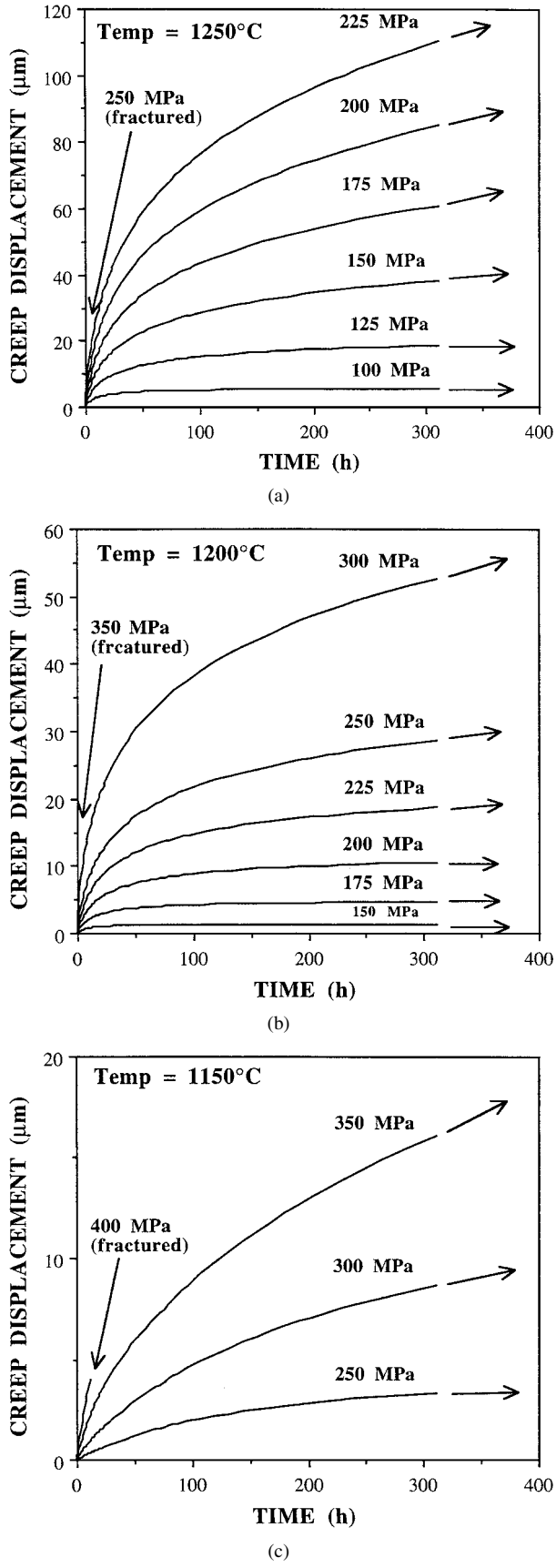

Figure 14 Simulated creep curves based on the advanced model combined with asymmetrical creep, (a) 1250°C; (b) 1200°C; (c) 1150°C.

(d) condition. The deflection rate data at 312-h mark or at rupture time, whichever is shorter, are shown in Fig. 15. In order to determine the stress exponent and activation energy (see Equation 8), Equation 28 is rewritten into the following form by including the temperature

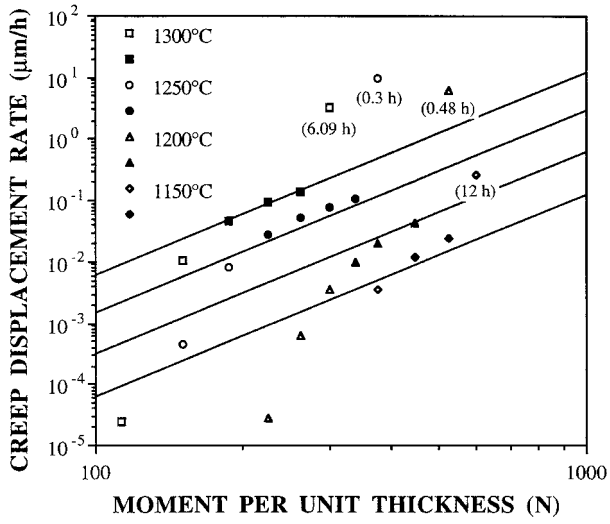

Figure 15 The creep rate data at 312 h, or earlier if the specimens rupture before 312 h, based on the simulations shown in Figs 8 and 14. The solid lines are the results of the regression analysis ($n = 3.3$, $Q = 563$ kJ/mole) based on the filled data.

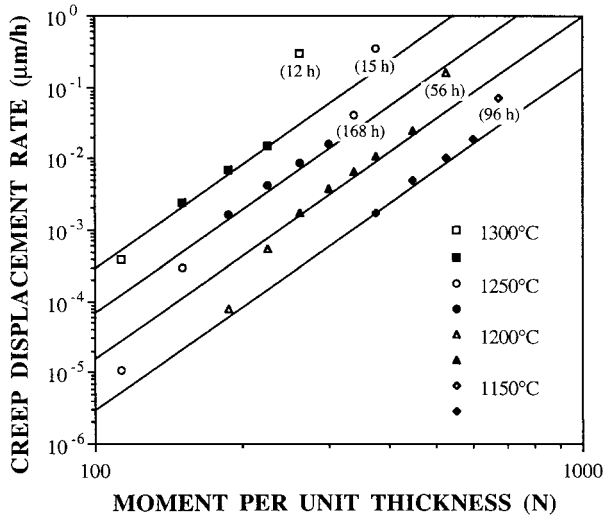

Figure 16 The creep rate data at 312 h, or earlier if the specimens rupture before 312 h, based on the power law creep model combined with asymmetrical creep. The solid lines are the results of the regression analysis ($n = 4.8$, $Q = 572$ kJ/mole) based on the filled data.

dependence term,

$$\ln\left(\frac{dU}{dt}\right) + \ln\left[\frac{32}{AL^2}\left(\frac{2n}{2n+1}\right)^n h^{2n+1}\right] = n\ln M - \frac{Q}{RT} \tag{38}$$

A simple linear multivariate regression analysis based on Equation 38 for the filled data leads to n and Q equal to 3.3 and 563 kJ/mole respectively. The results of the regression analysis are shown in Fig. 15 as solid straight lines. The open-symbol data are not used in the regression analysis for the same reasons discussed previously. Rupture lives under 4-point bending at 1150°C/450 MPa, 1200°C/350 MPa, and 1250°C/250 MPa are estimated to be 1.5 h, 0.48 h, and 0.3 h, respectively, based on case (d) condition. The short rupture lives predicted from the test conditions suggest that the slow-fracture tensile strengths may fall within the scatter of the flexural strengths indicated. In Ref. [11], the fracture strengths for tensile tests at a loading rate of 7.5 MPa/m were estimated to be 490, 393, and 279 MPa at 1150, 1200, and 1250°C, respectively. The agreement between the predicted tensile and flexural strength is respectable.

The preceding simulation study was repeated but using case (b) condition. Creep curves, not shown here, are simulated up to 312 h, and creep rates at 312 h are determined and shown in Fig. 16. Values of n and Q are determined to be 4.8 and 572 kJ/mole, respectively, based on the filled data points. The same exclusion rule has been applied to the unfilled data points. A deflection creep rate lower than 10^{-3} μm/h as indicated by the unfilled symbols accumulates less than 1 μm in 312 h of creep.

Finally, the creep displacements based on the symmetrical power law creep model, i.e., case (a), under various initial elastic stress distributions are also simulated as shown in Fig. 17. As would be expected, the slopes of the lines in the later stage of the creep should approach to a value of one. The creep rates as a function of the applied moments are shown in Fig. 18. Based on

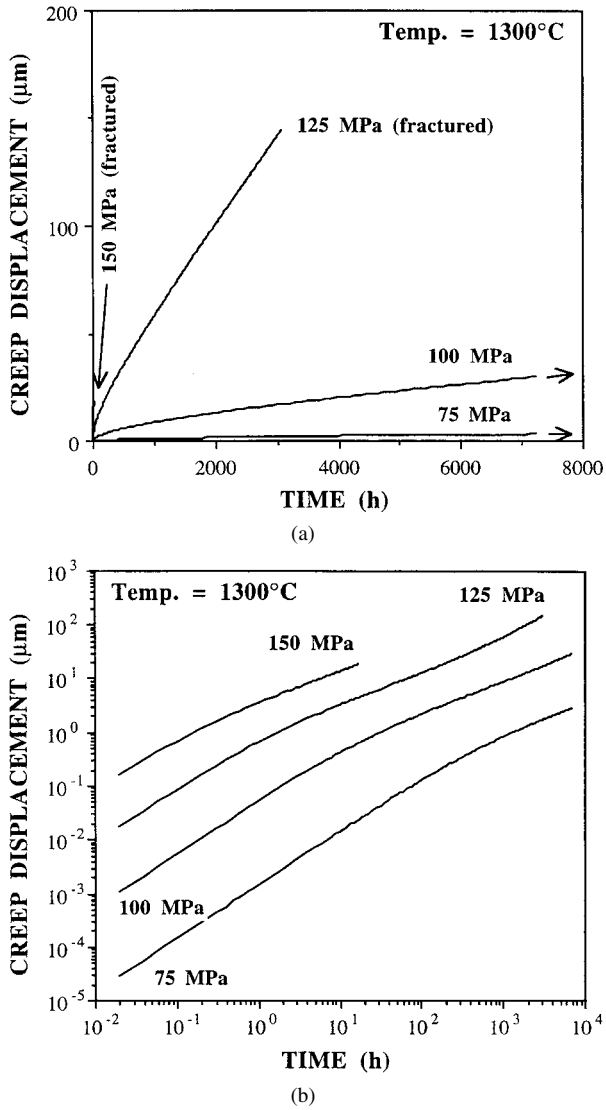

Figure 17 Simulated creep displacement based on the symmetrical power law creep model as a function of time. (a) linear scale; (b) log-log scale.

the creep rates at 312 h (square symbols in Fig. 18), two low-stress tests are still in transient stage at 312 h. The stress exponent is estimated to be 8.1 from the short-term data, and 12 based on the long-term data (circles)

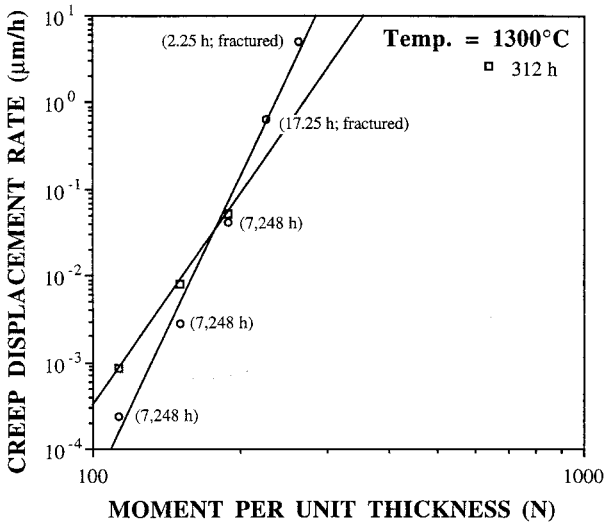

Figure 18 The creep rates as a function of the applied moments based on the simulations shown in Fig. 17.

which are determined from tests that are most likely in or approaching to steady state stage. The latter index value and the exponent of 12.6 in Equation 8 are in good agreement as would be expected.

6. Discussion

In the current study, two different material models were considered, namely, advanced model and power law creep model. For each model, two different cases were investigated, symmetrical creep versus asymmetrical creep. These two cases represent two extremes. The real material behavior is somewhere in between depending on the magnitude of compression creep. Since GN-10 appears to have little compression creep as shown in Fig. 2, the advanced model combined with asymmetrical creep is expected to give a reasonably realistic description of the behavior of CN-10 ceramic under four-point bending. Of course, the model can be further refined such as inclusion of the possible interaction between damage and creep [18], and even creep recovery [19]. However, the above mechanisms are assumed to play a minor role on the overall material response for GN-10 based on the available experimental evidence.

The analyses carried out in the current study demonstrated that the strees and strain fields in the specimen during a creep bend test vary with respect to both time and space in a very complicated way. For a given applied bending moment, the measured specimen deflection represents the averaged behavior due to these complicated stress and strain fields. Therefore, it is difficult to correlate the measured deflection with a particular stress state. The validity of the stress exponent (n) and activation energy (Q) extracted from the bend creep tests depends strongly on how close the underlying assumptions for the analysis is to reality. For example, in the current study, Hollenberg's analysis was used to extract n and Q which was based on the assumption that material behavior follows power law creep model and is symmetrical in tension and compression. Therefore it's not surprising that the n value estimated for case (a), i.e., 12, is close to the input value, i.e., 12.6. For the materials that have asymmetrical behavior in tension and compression, Hollenberg's analysis will of course lead to much lower value for n because the deflection represents the averaged response of large tension creep and little compression creep.

In Refs. [1, 4], besides the deflection, the indentation technique was also used to pinpoint the location of neutral axis and curvature rate. The tests had to be constantly interrupted and the process was laborious. More *in situ* measurements will of course be helpful for understanding and interpreting the bend test data. However, in this case, the major advantage of the bend test, namely, simplicity, is relinquished.

7. Conclusion

A general formulation for bending analysis under creep condition has been presented. The formulation is capable of embracing various material models. Through the numerical simulations a good understanding of the evolution of the deformation and stress fields inside the specimen during four-point bend creep testing has been achieved. The measured deflection in a bend creep test represents the averaged response to the inhomogeneous stress and strain distributions in the specimen. Hence, it is generally difficult to use the deflection data alone to extract intrinsic material information associated with a particular stress state from this type of test. The validity of the material parameters derived from these data depends on the validity of the assumptions that underlie the analysis. More *in situ* measurements to obtain information besides deflection, such as the location of the neutral axis and curvature etc., will be helpful for interpreting the bend test data. However, in this case, the major advantage of the bend test, namely, simplicity, is eradicated.

Acknowledgements

This research was sponsored by the U.S. Department of Energy (USDOE), Assistant Secretary for Conservation and Renewable Energy, Office of Transportation Technologies, as part of the Ceramic Technology Project of the Materials Development Program, under contract DE-AC05-84OR21400 with Martin Marietta Energy Systems, Inc.. Thanks are also due to Dr. K. C. Liu at Oak Ridge National Lab for providing Fig. 2 and many insightful inputs and suggestions.

References

1. C.-F. CHEN and T.-J. CHUANG, *J. Amer. Ceram. Soc.* **73** (1990) 2366.
2. H.-T. LIN and P. F. BECHER, *ibid.* **74** (1991) 1886.
3. R. B. THAYER and J.-M. YANG, *J. Mater. Sci.* **29** (1994) 693.
4. J. A. SALEM and S. R. CHOI, in Life Prediction Methodologies and Data for Ceramic Materials, ASTM STP 1201, 1994, edited by C. R. Brinkman and S. F. Duffy, p. 84.
5. A. RENDTEL and H. HÜBNER, *J. Amer. Ceram. Soc.* **81** (1998) 1109.
6. G. W. HOLLENBERG, G. R. TERWILLIGER and R. S. GORDON, *ibid.* **54** (1971) 196.
7. I. FINNIE, *ibid.* **49** (1996) 218.
8. P. K. TALTY and R. A. DIRKS, *J. Mater. Sci.* **13** (1978) 580.
9. T.-J. CHUANG, *ibid.* **21** (1986) 165.
10. J. L. DING, K. C. LIU, C. R. BRINKMAN and S. B. LIN, *J. Amer. Ceram. Soc.* **78** (1995) 3057.

11. K. C. LIU, C. R. BRINKMAN, J. L. DING and S. B. LIN, *ASME J. Engineering for Gas Turbines and Power* **119** (1997) 200.
12. J. L. DING, K. C. LIU and C. R. BRINKMAN, *Ceramic Engineering & Science Proceedings* **17**(3) (1996) 15.
13. J. L. DING, K. C. LIU, K. L. MORE and C. R. BRINKMAN, *J. Amer. Ceram. Soc.* **77** (1994) 867.
14. K. C. LIU, C. O. STEVENS and C. R. BRINKMAN, in Proceedings of 41st ASME Gas Turbine and Aeroengine Congress, Birmingham, UK, June 1996.
15. K. J. YOON, S. M. WIEDERHORN and W. E. LUECKE, *J. Amer. Ceram. Soc.* **83** (2000) 2017.
16. T.-J. CHUANG, *ibid.* **81** (1998) 2749.
17. T.-J. CHUANG, S. M. WIEDERHORN and C. F. CHEN, in Proc. 3rd Int. Conf. On Creep and Fracture of Engineering Materials and Structures, edited by B. Wilshire and R. W. Evans (Institute of Metals, London, 1987).
18. C. R. BLANCHARD and K. S. CHAN, *J. Amer. Ceram. Soc.* **76** (1993) 1651.
19. J. L. DING and W. N. FINDLEY, *ASME J. Appl. Mech.* **51** (1984) 125.

Received 14 August 2001
and accepted 20 June 2002